

## EFFECT OF CYCLE COUNT IN SILAR DEPOSITION OF COUNTER ELECTRODE ON THE PERFORMANCE OF QUATERNARY QUANTUM DOT SENSITIZED SOLAR CELL

N. SINGH<sup>a</sup>, J. SHARMA<sup>a</sup>, S. K. TRIPATHI<sup>a, b,\*</sup>

<sup>a</sup>Centre for Nano Science and Technology, Panjab University Chandigarh  
160014, India

<sup>b</sup>Centre for Advanced Studies in Physics, Panjab University Chandigarh 160014,  
India

Cu-Ni-S alloyed films of different thicknesses were prepared by varying the number of cycles in SILAR deposition and were used for the application as Counter Electrode in QDSSCs. For device fabrication, titanium dioxide films were used as a photo-anode layer, Cu<sub>2</sub>ZnSnS<sub>4</sub> quaternary quantum dots as a sensitizer, and polysulfide electrolyte was used as Redox mediator. The effect of number of SILAR cycles on the electrical and electrochemical parameters was studied with V-I characteristic curve and electrochemical impedance spectroscopy. The device incorporating counter electrode deposited by 10 SILAR cycles performed best among other devices because of its lowest impedance parameters.

(Received November 19, 2019; Accepted March 22, 2020)

*Keywords:* QDSSC, SILAR synthesis, Quaternary quantum dots, Cu-Ni-S alloy, Counter electrode.

### 1. Introduction

Increased global energy demands and global warming are major factors that are pushing research to the field of renewable energy sources. Conventional energy sources are not only affecting the nature but also limited in quantity. From the past few decades, every possible non-conventional energy source is being explored. Like, nuclear fission reactors, wind energy, geothermal energy, and solar energy have become remarkable alternate energy sources [1]. Whereas wave energy, tidal energy, fuel cells, nuclear fusion reactors are new in the field of power generation. Further, every energy source has its limitations like nuclear energy waste restricts its overuse [2]. Wind energy, geothermal energy, wave energy, and tidal energy is limited to geographical conditions [3, 4]. Nuclear fusion reactors are still in the initial stage [5].

The availability of solar energy in most of the land and throughout the year makes it a suitable choice as an alternate energy source. Solar energy is used in different ways to harness energy. Passive solar [6] and active solar [7] are two broad branches to harness solar energy. In active solar energy, reflectors are used to concentrate light on the water chamber (collector/pipes). This super-heated water is circulated with the help of water pumps and then made to run turbines to generate electricity. Passive solar energy includes photovoltaic (PV) devices which transduce light directly into the usable electric form. PV devices are more versatile and comparably cheaper [8].

There exist four generations of PV devices. First-generation PV cells consist of single/multi-crystalline silicon wafers. Their efficiency is limited by the narrow band of silicon and they were significantly costly initially [9]. Second-generation PV devices are thin-film based devices. They are cheaper than the first generation and have a higher absorption coefficient. But these devices possess environmental concerns [10]. Dye-sensitized solar cells (DSSC), quantum dot sensitized solar cells (QDSSC), and organic solar cells are third-generation of solar cells. They

---

\*Corresponding author: surya@pu.ac.in

have several advantages over the first two generations of devices. Like, readily available material, low-cost fabrication processes, and versatile applications make them a great choice as a PV device [11].

QDSSCs have four layers sandwiched together in the presence of liquid polysulfide electrolyte. As shown in figure 1, fluorine-doped tin oxide (FTO) is used as a substrate. On one substrate photoanode material is deposited and on other substrate catalysts or counter electrode (CE) is deposited. FTO with photoanode is then treated to adsorb sensitizers over it. With a drop of polysulfide electrolyte, both FTOs are then sandwiched together. The basic working of QDSSC and DSSC is the same except for the choice of sensitizers, electrolytes, and CEs. In QDSSC quantum dots (QD) acts as sensitizers and are adsorbed over photoanode material. Sensitizers are the materials which on being exposed to sunlight create electron-hole pair. Electrons excited by light are taken by the photoanode materials [12].

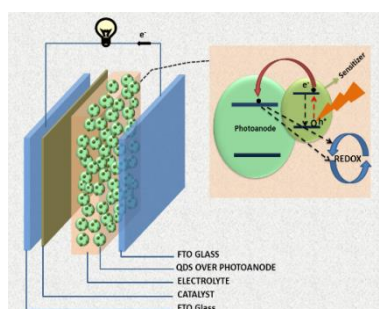


Fig. 1. Schematic diagram for QDSSC device; (Inset) electron transfer mechanism between QD and photoanode material (Black arrows representing electron-hole recombination).

Photoanode materials are generally nanoparticles with wide bandgap like titanium dioxide ( $\text{TiO}_2$ ) [13] and Zinc oxide ( $\text{ZnO}$ ) [14]. They have bandgap which is usually  $> 3$  eV and conduction band lying slightly lower than that of the bandgap of sensitizer material. This wide-bandgap restricts excited electrons from falling back to the valence band of sensitizer [15]. Extracted electrons are then pushed to the external circuit through FTO. Further, electrolyte takes up holes from the sensitizers through a redox reaction. The electrolyte is then recharged by CE which acts as a catalyst to transfer electrons from the FTO. In practical conditions, excited electrons may suffer recombination with holes via three routes. (i) From the conduction band of sensitizer to the valence band of the sensitizer. (ii) From the conduction band of photoanode to the valence band of sensitizer. (iii) From the conduction band of photoanode to the redox couple. These recombinations degrade device performance [16].

For good device performance, CE must be able to transfer charge carriers swiftly so that electron-hole recombination can be reduced. Catalyst plays an important role in the removal of holes from the electrolyte swiftly. It reduces electrolyte by providing electrons from the external circuit [17]. The choice of CE/catalyst solely depends on the redox couple opted for the device [18]. Platinum [19], carbon materials [20], conductive polymers [21-23], metal substrates and various composites have been used as CE [24, 25]. Platinum CE is favored for DSSCs as it performs well with the poly-iodide electrolyte. But in the case of QDSSC, the poly-sulfide electrolyte is used which corrodes the platinum or any metal CE. Therefore different types of metal-sulfide and their composites are used. Copper sulfide ( $\text{CuS}$ ), nickel sulfide ( $\text{NiS}$ ) [26], cobalt sulfide ( $\text{CoS}$ ) [27],  $\text{CuS/NiS}$  [28] and  $\text{CuS/CoS}$  [29] are some of the metal sulfide/composites used as CE for QDSSCs. There are different deposition techniques to deposit these CE materials onto the FTO/substrate like chemical bath deposition (CBD), physical vapor decomposition (PVD), electrochemical deposition, chemical vapor deposition (CVD), chemical reduction, hydrothermal reaction, and sputtering technique [30].

Enhanced CBD or successive ionic layer adsorption reaction (SILAR) is an easy approach to deposit metal-sulfide over FTO [31]. It has the following advantages over other deposition

techniques. (i) Unlike PVD, CVD, Sputtering technique it does not require vacuum processing, it makes processing costs lower. (ii) The rate of deposition and size of the deposited material can be controlled easily. (iii) Unlike sputtering and PVD it does not heat material which is a crucial factor in thin layers. (iv) The thickness of the films can be easily controlled. These merits make SILAR deposition a great choice for the fabrication of CE [32].

Fig. 2 represents a basic SILAR cycle. It involves four steps. First of all, the substrate is dipped into a cationic solution, followed by rinsing in deionized (DI) water. Then the substrate is dipped into an anionic solution followed by DI water rinsing. By varying the cycle duration, molar concentration, and the number of cycles, the desired thickness of the films can be achieved.

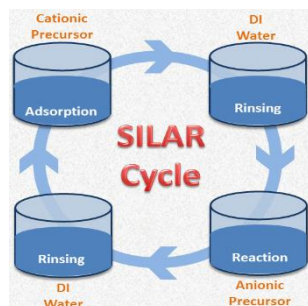


Fig. 2. Various steps involved in a cycle of SILAR synthesis technique.

As discussed earlier sulfides of Cu and Ni are successful in delivering high catalytic activity as counter electrode material in QDSSC devices [33]. They have exhibited good conjugation with poly-sulfide electrolyte. In this paper, we have deposited Cu-Ni-S alloy as CE on FTO for application as a counter electrode in the device. SILAR deposition technique was opted to deposit Cu-Ni-S film over FTO. Further to observe the effect of the number of SILAR cycles on the device performance, numbers of SILAR cycles for deposition of CE were changed. Subsequently, due to an increase in the number of cycles the thickness variation in CE was observed. For the realization of QDSSC device, other components of the device were chosen from the literature review and were made standard across different CE films. For its superior performance, anatase  $\text{TiO}_2$  nanoparticles prepared by sol-gel technique were used as photoanode material. Similarly,  $\text{Cu}_2\text{ZnSnS}_4$  quaternary QDs were opted as sensitizer material for their non-toxic behavior. As the compatibility of polysulfide redox couple is well established for metal-sulfide CE, it was chosen as an electrolyte for the device. To observe the variation in thickness of CE by varying the number of SILAR cycles, scanning electron micrograph (SEM) images were taken and analyzed. Further to confirm the constituents of CE, wavelength dispersive X-ray fluorescence (WDXRF) analysis was done. To characterize the prepared photoanode material, X-ray diffraction (XRD) spectra were taken for the CE coated FTO glass and  $\text{TiO}_2$  nanoparticles. Successful binding of QDs over  $\text{TiO}_2$  nanoparticles was observed with transmission electron microscopy (TEM). Final devices were tested with solar-simulator and analyzed to compare the effect of CE thickness on the photovoltaic performance of the QDSSCs

## 2. Experimental methods (synthesis)

$\text{TiO}_2$  nanoparticles were synthesized by the sol-gel synthesis technique [34]. Further, water-soluble quaternary copper-zinc-tin-sulfide ( $\text{Cu}_2\text{ZnSnS}_4$ ) QD were synthesized hydrothermal method proposed by Das et al. [35].  $\text{TiO}_2$  films were immersed in  $\text{Cu}_2\text{ZnSnS}_4$ -Water dispersions for 8 hours. Polysulfide electrolyte was obtained by adding 1M  $\text{Na}_2\text{S}$ , 2M elemental sulfur, and 0.2M  $\text{NaOH}$  to the mixture of water and ethanol in the ratio of 8:2. Counter electrode films were prepared by SILAR deposition technique. As a cationic source, 0.5M nickel acetate and 0.5M copper acetate were used, 1M thioacetamide was opted as an anionic source. Reaction time was

kept 30 sec and the washing time was set 45 sec. Four different films were prepared named C5, C10, C15 and C20 based on the respective number of SILAR cycles that are 5 cycles, 10 cycles, 15 cycles and 20 cycles. Devices were prepared by sandwiching active layer (QD coated TiO<sub>2</sub> film) and counter electrodes with polysulfide electrolyte. To increase readability and understanding, devices have been also named as C5, C10, C15, C20, and FTO with respect to CE used in the devices.

### 2.1. Instrumentation

Scanning electron microscopy (SEM) images were taken with Zeiss, EVO18 of the CE coated FTO films. X-ray diffraction (XRD) spectra were observed for the TiO<sub>2</sub> powder and CE/FTO films with Rigaku, Miniflex300 benchtop X-ray diffractometer. WDXRD studies were carried out on C10 CE with WD-XRF Spectrometer Model-S8 TIGER Bruker. Transmission Electron Microscope (TEM) images of QD coated TiO<sub>2</sub> nanoparticles were taken with the Tecnai, G20 (FEI). Electrical Impedance Spectroscopy was performed on Metrohm C-V tester. For photovoltaic characteristics, prepared devices were tested with the PET SS80AAA-EM solar simulator with a 300-watt xenon arc lamp and AM 1.5G filter. The input power of the simulator was 100 mW/cm<sup>2</sup> ±15% and the active area of the prepared devices was 0.5 cm<sup>2</sup>.

### 3. Results and discussion

Working electrode and counter electrode are two crucial components of a QDSSC device. As the literature shows that TiO<sub>2</sub> nanoparticles are one of the best choices for the device due to transparency to white light and mesoporous structure [36]. That is why it has been adapted as photo-anode material in our device. To confirm the synthesis of TiO<sub>2</sub> nanoparticles and the size of the synthesized nanoparticles XRD spectrum was taken.

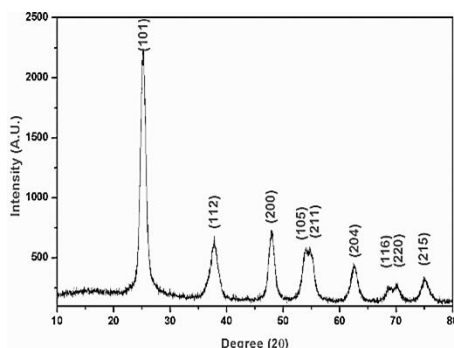


Fig. 3. XRD spectrum for the anatase phase of TiO<sub>2</sub> nanoparticles.

Fig. 3 shows the XRD spectrum for synthesized TiO<sub>2</sub> nanoparticles. Peaks present at  $2\theta = 25.20^\circ$ ,  $38.57^\circ$ ,  $48.04^\circ$ ,  $53.07^\circ$ ,  $62.69^\circ$ ,  $68.76^\circ$ ,  $70.30^\circ$  and  $75.05^\circ$  are respective peaks for the (101), (112), (200), (105), (211), (204), (116), (220) and (215) planes of the anatase phase of TiO<sub>2</sub> nanoparticles. All the peaks are in good agreement with the PDF card no. 9015929. Anatase phase is considered best for the sensitized solar cells. Electron diffusion coefficient in anatase TiO<sub>2</sub> is higher than any other photoanode material [37]. From the FWHM the crystallite size was calculated using the Debye-Scherrer formula.

$$D = 0.9\lambda/\beta\cos\theta \quad (1)$$

where D = crystallite Size,  $\lambda$  = wavelength of the X-Ray source which is 1.5406 Å for copper source,  $\beta$  = FWHM and  $\theta$  = angle between the incident beam and the scattered X-ray. The average size has been calculated by taking the mean of all observed crystallite sizes. The observed

crystallite size was  $\sim 20$  nm. The size of the nanoparticles was also confirmed from the TEM images of the QD loaded  $\text{TiO}_2$  nanoparticles shown in figure 4. Clear visual evidence of finely distributed QD over  $\text{TiO}_2$  with size  $\sim 2.5$  nm to 5 nm can be seen in the TEM image. This kind of distribution of QD is crucial for fast charge transportation from sensitizer to the photo-anode material. As shown in figure QD adhered to  $\text{TiO}_2$  are in good numbers without any binders. Also, the contrast in the TEM image suggests mesoporous morphology which facilitates greater surface area for adsorption of QD.

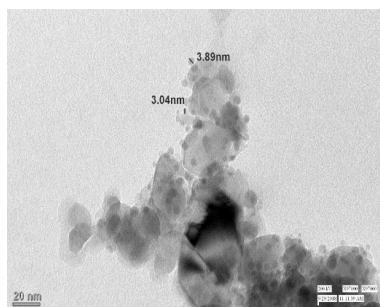


Fig. 4. TEM micrograph for QD loaded mesoporous  $\text{TiO}_2$  nanostructure

Fig. 5 shows a cross-sectional view of CE coated FTO glass as an SEM micrograph. These images were taken to observe variation in the thickness of the CE films with an increased number of SILAR cycles. For C5 the thickness was 644 nm which increased to 3.8  $\mu\text{m}$  for C10 and 7.5  $\mu\text{m}$  for C15. Up to 15 cycles the thickness increased linearly with the number of cycles. But for the C20 the thickness increased non-linearly to 24.3  $\mu\text{m}$ . This may be due to the high degree of supersaturation in the SILAR process, where supersaturation is the ratio of the ionic product to the solubility product [38]. The thickness of these films includes the thickness of FTO film which is  $\sim 180$  nm. As the gold was deposited over the CE/FTO films it was not possible to distinguish between CE and FTO.

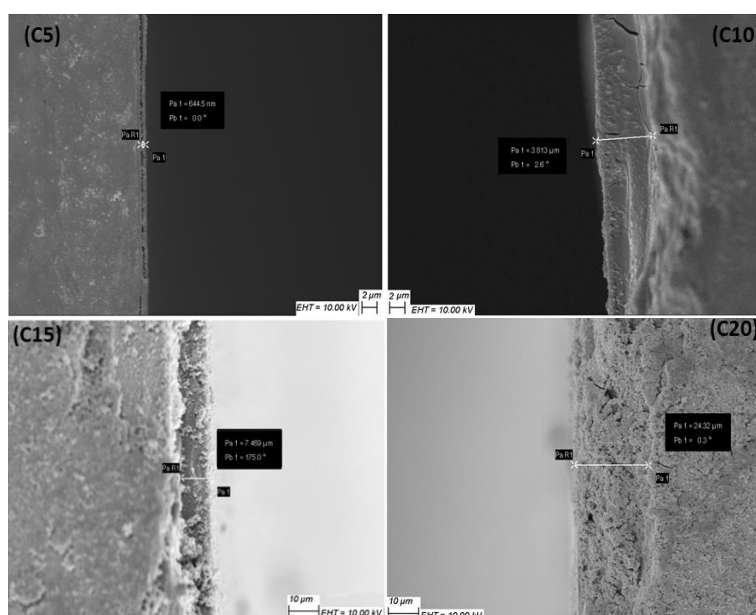


Fig. 5. SEM micrograph for different CE films named C5, C10, C15 and C20 for respective 5, 10, 15 and 20 number of SILAR cycles.

Fig. 6 illustrates the XRD spectra for CE coated FTO glass. XRD was done to observe the effect of increased SILAR cycles on the crystallite size of alloyed CuNiS films. In C5 absence of the peaks corresponding to the alloyed film suggests no or very less crystal formation. In C10 and C15 peaks present at  $2\theta = 22.15^\circ$  and  $23.40^\circ$  belongs to the alloyed CuNiS film with crystalline size 78 nm and d-spacing 0.38 nm for the intense peak. Crystallite size and d-spacing were calculated by the Deby-Scherrer formula. Peak positions were matched with PDF cards related to CuS, Cu<sub>2</sub>S, NiS, and NiS<sub>2</sub> but no match was found. Peak present at  $2\theta = 23.40^\circ$  faded in C20 and a new peak emerged at  $2\theta = 20.14^\circ$  with d-spacing 0.44 nm and crystalline size 86.6 nm. It suggests the formation of a new phase of Cu-Ni-S alloy.

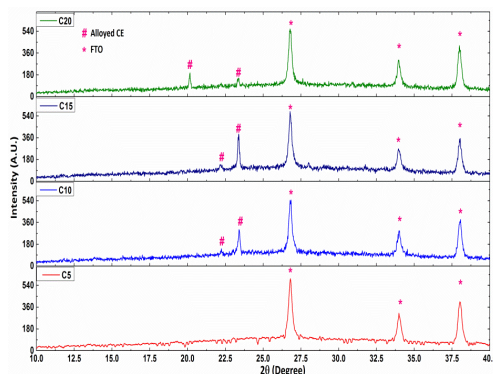


Fig. 6. XRD spectra for CE/FTO with the different number of cycles, named C5, C10, C15 and C20 for 5, 10, 15 and 20 numbers of cycles respectively.

In Fig. 7, EDXRF spectrum with for the CE material is shown and the compositional values for the constituent material have been listed in the table inserted in the EDXRF spectrum. Copper and sulfur were present almost in the same composition which is ~45 atomic % but the nickel was present in less. This may be due to less Van der Waals radius ( $r_v$ ) for the copper ions. As the SILAR process involves adsorption of ion, less  $r_v$  facilitates adsorption of more copper ion than the nickel ions.

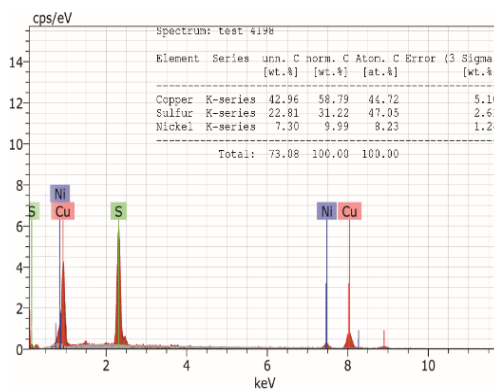


Fig. 7 EDX spectra for alloyed CuNiS CE film, (inset) table for the normalized value of the constituent elements

The critical parameters for electrode layers are obtained from EIS (Electrochemical Impedance Spectroscopy). It is used to calculate the effect of electrical impedance (reactance and resistance) in the electrochemical performance of the electrodes. Fig. 8 shows Nyquist plot between real and imaginary parts of the EIS data with an equivalent circuit.

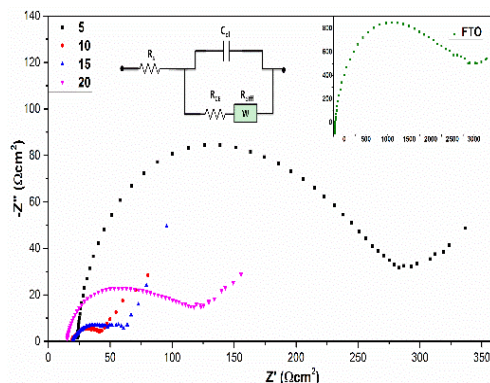


Fig. 8. Nyquist graph for EIS data for counter electrodes prepared by the different number of cycles and inset Nyquist plot for EIS data of bare FTO glass electrode.

Various parameters obtained from the fitting of EIS data with respect to the equivalent circuit (shown in Fig. 8) are listed in Table 1.  $R_s$  denotes series resistance which is also known as electrode resistance,  $R_{CE}$  is electrolyte resistance,  $R_{diff}$  is diffusion layer resistance which is also known as Warburg resistance, and  $C_{dl}$  is double-layer capacitance.

Table 1 also lists electrical characteristics for the devices prepared using FTO, C5, C10, C15 and C20 films as a counter electrode, where  $V_{oc}$  is for open-circuit voltage,  $I_{sc}$  stands for short circuit current, FF denotes fill factor of the device and  $P_{max}$  is for maximum power output for the device. FF of the devices is calculated with the following equation 1. The V-I characteristic curves for various devices are shown in Fig. 9.

$$\text{Fill Factor} = \frac{P_{max}}{I_{sc} * V_{oc}} \quad (2)$$

$$\text{Where, } P_{max} = V_{max} * I_{max} \quad (3)$$

Table 1. VI characteristics of device with five different counter electrodes (i) Bare FTO (ii) C5 (iii) C10 (iv) C15 (v) C20.

Device/ CE	$V_{oc}$ (mV)	$I_{sc}$ (mA)	FF (%)	$P_{max}$ ( $\mu$ W)	$R_s$ ( $\Omega$ cm <sup>2</sup> )	$R_{CE}$ ( $\Omega$ cm <sup>2</sup> )	$R_{diff}$ ( $\Omega$ cm <sup>2</sup> )
TiO <sub>2</sub> /QD/ FTO	51.7	0.18	25	4.8	45.4	3598	1974
TiO <sub>2</sub> /QD/ C5	144.7	0.37	25	59.5	26.7	213	92
TiO <sub>2</sub> /QD/ C10	249.3	0.62	30	70.2	19.8	16.7	39
TiO <sub>2</sub> /QD/ C15	195.6	0.36	29	21.7	20.9	34.9	44
TiO <sub>2</sub> /QD/ C20	100.1	0.18	25	5.2	20.7	88.4	65

By varying the thickness of the CE films, a significant change in the device performance was observed. In the Device performance improved from FTO to C10 and then deteriorated in C15 and C20. Device C15 exhibited best FF owing to the best values for the  $I_{sc}$  and  $V_{oc}$ . Maximum value for  $P_{max}$  i.e. 70 $\mu$ W, was obtained for device C10.

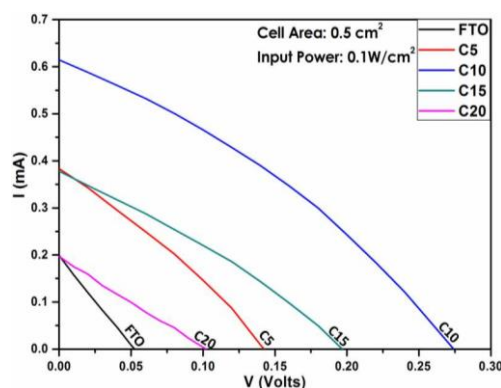


Fig. 9. V-I characteristic curves for different devices with five different counter electrodes (i) Bare FTO (ii) C5 (iii) C10 (iv) C15 (v) C20.

As shown in the EIS plot, high impedance was observed in bare FTO electrode, large values for  $R_{CE}$  and  $R_{diff}$  are due to the low catalytic activity of the bare FTO. Therefore the device performed worst. It may be caused by slow redox reaction kinetics with the electrolyte which requires swift charge transfer between redox couple and the external circuit [39].

In device C5 the device performance improved. Significant improvement was observed in the  $V_{oc}$  and  $I_{sc}$ , this change is due to the drastic improvement in the electrolytic behavior of the CE. The value for  $R_{CE}$  lowers down to  $213 \Omega\text{cm}^2$  from  $3598 \Omega\text{cm}^2$  which can be attributed to the electrolytic conductance of CuS/NiS alloyed CE. Also, the diffusion resistance decreased significantly which reflects faster electron transfer between CE material and electrolyte [40]. Due to this, there must be a decrease in electron-hole recombination which leads to  $V_{oc}$  of the device C5 improved significantly. Also, due to the fast diffusion of electrons into the electrolyte, electron-hole recombination at the interface between the poly-sulfide electrolyte and semiconducting materials decreases.

In device C10 further improvement in electrochemical behavior was observed. Values for  $R_s$ ,  $R_{CE}$ , and  $R_{diff}$  were at the minimum for C10 CE. Where  $R_s$  corresponds to the series resistance of the CE. Lower values of  $R_s$  are due to better connectivity of CE material and FTO glass [41]. Further improved value of the  $R_{CE}$  and  $R_{diff}$  caused by a better CE-electrolyte interface resulted in improvement in electrical parameters of the device C10. The values for  $V_{oc}$  and  $I_{sc}$  almost doubled which caused better performance than the C5 device.

In device C15 and C20 the values for  $R_{CE}$ , and  $R_{diff}$  were deteriorated causing a decrease in the electrical characteristic of the devices.  $R_{CE}$  should be low to effectively transfer charge carriers from the external circuit to the poly-sulfide electrolyte. As shown in figure 5, due to an increase in the number of cycles, the thickness of the CE layer increases and the CE becomes brittle in C15 and C20. This may have caused an increase in the impedance of the CE layer. Therefore with the increased values of  $R_{CE}$ , and  $R_{diff}$ , the  $V_{oc}$  dropped drastically in the C15 and C20. Also,  $I_{sc}$  degraded due to the increased value of  $R_{diff}$  in C15 and C20. It results in slow diffusion of electrons through the electrolyte which further leads to increased electron-hole recombination.

#### 4. Conclusions

The XRD spectrum of  $\text{TiO}_2$  nanoparticles exhibited a successful synthesis of the anatase phase with average crystallite size  $\sim 20$  nm. TEM image displayed successful binding of quaternary CZTS QD of  $\text{TiO}_2$  nanoparticles without any chemical binders. Also, the TEM image provided visual proof for finely distributed QD over  $\text{TiO}_2$  nanoparticles, which is crucial for the fast transportation of charge carriers. Cross-sectional SEM images of CE films displayed growth of CuNiS alloyed CE over FTO with the increasing number of SILAR cycles. With the increased

number of the SILAR cycles, the thickness of the CE films increased. Linear growth was observed up to 15 cycles but in CE with 20 cycles the growth was sharp. XRD of CE films suggested the formation of crystalline CuNiS alloyed material as no particular peak for CuS, Cu<sub>2</sub>S or NiS was found.

The size of the CE material was calculated as ~78 nm. Further, a new peak emerged in C20 film with crystallite size ~86 nm suggesting the formation of a new phase. The presence of nickel, copper, and sulfur in the CE films was confirmed by WDXRF analysis. From the observed PV characteristics of the device, device performance was improved in device C5 and C10 due to the improved electrochemical behavior of the CE films. But in the devices C15 and C20, device characteristics degrade, which resulted in the increased values of  $R_{CE}$  and  $R_{diff}$ . Device C10 performed best among other devices with maximum power output i.e. 70 $\mu$ W. Approximately 15-fold increase in output power was observed in the C10 device than the device with bare FTO as CE. This is due to the faster diffusion of charge carriers to the electrolyte by CE material and decreased electron-hole recombination in device with C10 CE.

### Acknowledgments

Author Navjot Singh wants to thank UGC for providing fellowship to carry out research.

### References

- [1] P. A. Owusu, S. Asumadu-Sarkodie, *Cogent Engineering* **3**(1), (2016).
- [2] J. P. Christodouleas, R. D. Forrest, C. G. Ainsley, Z. Tochner, S. M. Hahn, E. Glatstein, *N Engl J Med* **364**(24), 2334 (2011).
- [3] D. Scholten, R. Bosman, *Technological Forecasting and Social Change* **103**, 273 (2016).
- [4] R. Heinberg, *European Business Review* **17**(5), null (2005).
- [5] A. M. Bradshaw, T. Hamacher and U. Fischer, *Fusion Engineering and Design* **86**(9-11), 2770 (2011).
- [6] S. Stevanovic, *Renewable & Sustainable Energy Reviews* **25**, 177 (2013).
- [7] A. G. Hestnes, *Sol Energy* **67**(4-6), 181 (1999).
- [8] X. Guo, H. Li, B. Y. Ahn, E. B. Duoss, K. J. Hsia, J. A. Lewis, R. G. Nuzzo, *Proc Natl Acad Sci U S A* **106**(48), 20149 (2009).
- [9] B. Parida, S. Iniyar, R. Goic, *Renewable & Sustainable Energy Reviews* **15**(3), 1625 (2011).
- [10] V. Fthenakis, *Renewable & Sustainable Energy Reviews* **13**(9), 2746 (2009).
- [11] A. J. Nozik, M. C. Beard, J. M. Luther, M. Law, R. J. Ellingson, J. C. Johnson, *Chem Rev* **110**(11), 6873 (2010).
- [12] V. T. Chebrolu, H. J. Kim, *Journal of Materials Chemistry C* **7**(17), 4911 (2019).
- [13] M. Shakeel Ahmad, A. K. Pandey, N. Abd Rahim, *Renewable and Sustainable Energy Reviews* **77**, 89 (2017).
- [14] R. Vittal, K. C. Ho, *Renewable & Sustainable Energy Reviews* **70**, 920 (2017).
- [15] K. Fan, J. G. Yu, W. K. Ho, *Materials Horizons* **4**(3), 319 (2017).
- [16] S. K. Tripathi, M. Rani, N. Singh, *Electrochimica Acta* **167**, 179 (2015).
- [17] B. K. Koo, D. Y. Lee, H. J. Kim, W. J. Lee, J. S. Song, H. J. Kim, *Journal of Electroceramics* **17**(1), 79 (2006).
- [18] P. Balraju, P. Suresh, M. Kumar, M. S. Roy, G. D. Sharma, *Journal of Photochemistry and Photobiology a-Chemistry* **206**(1), 53 (2009).
- [19] Y. L. Lee, C. L. Chen, L. W. Chong, C. H. Chen, Y. F. Liu, C. F. Chi, *Electrochemistry Communications* **12**(11), 1662 (2010).
- [20] Z. Huang, X. H. Liu, K. X. Li, D. M. Li, Y. H. Luo, H. Li, W. B. Song, L. Q. Chen, Q. B. Meng, *Electrochemistry Communications* **9**(4), 596 (2007).
- [21] B. H. Fan, X. G. Mei, K. Sun, J. Y. Ouyang, *Applied Physics Letters* **93**(14), 143103 (2008).

- [22] Q. H. Li, J. H. Wu, Q. W. Tang, Z. Lan, P. J. Li, J. M. Lin, L. Q. Fan, *Electrochemistry Communications* **10**(9), 1299 (2008).
- [23] J. H. Wu, Q. H. Li, L. Q. Fan, Z. Lan, P. J. Li, J. M. Lin, S. C. Hao, *Journal of Power Sources* **181**(1), 172 (2008).
- [24] H. C. Sun, D. Qin, S. Q. Huang, X. Z. Guo, D. M. Li, Y. H. Luo, Q. B. Meng, *Energy & Environmental Science* **4**(8), 2630 (2011).
- [25] X. Xin, M. He, W. Han, J. Jung, Z. Lin, *Angew Chem Int Ed Engl* **50**(49), 11739 (2011).
- [26] N. Singh, P. Siwatch, A. Arora, J. Sharma, S. K. Tripathi, *AIP Conference Proceedings* **1953**, 030159 (2018).
- [27] J. Y. Lin, J. H. Liao, T. C. Wei, *Electrochemical and Solid State Letters* **14**(4), D41 (2011).
- [28] H. J. Kim, S. M. Suh, S. S. Rao, D. Punnoose, C. V. Tulasivarma, C. V. V. M. Gopi, N. Kundakarla, S. Ravi, I. K. Durga, *Journal of Electroanalytical Chemistry* **777**, 123 (2016).
- [29] Z. Yang, C. Y. Chen, C. W. Liu, C. L. Li, H. T. J. A. E. M. Chang, **1**(2), 259 (2011).
- [30] S. Thomas, T. G. Deepak, G. S. Anjusree, T. A. Arun, S. V. Nair, A. S. Nair, *Journal of Materials Chemistry A* **2**(13), 4474 (2014).
- [31] J. G. Radich, R. Dwyer, P. V. J. T. J. o. P. C. L. Kamat, **2**(19), 2453 (2011).
- [32] H. M. Pathan, C. D. Lokhande, *Bulletin of Materials Science* **27**(2), 85 (2004).
- [33] Y.-S. Lee, C. V. Gopi, M. Venkata-Haritha, S. S. Rao, H.-J. Kim, *Journal of Photochemistry and Photobiology A: Chemistry* **332**, 200 (2017).
- [34] M. Rani, S. J. Abbas, S. Tripathi, *Materials Science and Engineering: B* **187**, 75 (2014).
- [35] S. Das, I. Alam, J. Raiguru, B. V. R. S. Subramanyam, P. Mahanandia, *Physica E-Low-Dimensional Systems & Nanostructures* **105**, 19 (2019).
- [36] B. Tan, Y. Wu, *J Phys Chem B* **110**(32), 15932 (2006).
- [37] K. Srinivas, K. Yesudas, K. Bhanuprakash, V. J. Rao, L. Giribabu, *The Journal of Physical Chemistry C* **113**(46), 20117 (2009).
- [38] C. Lokhande, B. Sankapal, H. Pathan, M. Muller, M. Giersig, H. Tributsch, *Applied surface science* **181**(3-4), 277 (2001).
- [39] N. Balis, V. Dracopoulos, K. Bourikas, P. Lianos, *Electrochimica Acta* **91**, 246 (2013).
- [40] K. Yang, Y. Wang, A. Jain, J. Kumar, *Journal of Macromolecular Science, Part A* **44**(12), 1261 (2007).
- [41] Z. Liu, M. Zhang, X. Xu, F. Cai, H. Yuan, L. Bu, W. Li, A. Zhu, Z. Zhao, M. Wang, *Journal of Materials Chemistry A* **3**(47), 24121 (2015).